



Science Arts & Métiers (SAM)

is an open access repository that collects the work of Arts et Métiers Institute of Technology researchers and makes it freely available over the web where possible.

This is an author-deposited version published in: <https://sam.ensam.eu>
Handle ID: <http://hdl.handle.net/10985/24975>



This document is available under CC BY license

To cite this version :

Lucas LAPOSTOLLE, Léo MORIN, Katell DERRIEN, Laurent BERTHE, Olivier CASTELNAU - Exact expressions of the uniaxial perfectly elasto-plastic stress wave and induced mechanical fields in the case of a finite impact: application to laser shock peening - Comptes Rendus. Mécanique - Vol. 351, n°G2, p.459-484 - 2023

Any correspondence concerning this service should be sent to the repository

Administrator : scienceouverte@ensam.eu





Research article / Article de recherche

Exact expressions of the uniaxial perfectly elasto-plastic stress wave and induced mechanical fields in the case of a finite impact: application to laser shock peening

Expressions exactes de l'onde de contrainte élasto-plastique uniaxiale et des champs mécaniques induits dans le cas d'un impact fini : application au grenaillage laser

Lucas Lapostolle^{①,*}, Léo Morin^{①,b}, Katell Derrien^{①,a}, Laurent Berthe^{①,a}
and Olivier Castelnau^{①,a}

^a PIMM, Arts et Metiers Institute of Technology, CNRS, Cnam, HESAM University,
151 boulevard de l'Hopital, 75013, Paris, France

^b University of Bordeaux, CNRS, Arts et metiers Institute of Technology, Bordeaux INP,
I2M, Bordeaux, F-33400, Talence, France

E-mails: lucas.lapostolle@ensam.eu, lucas.lapostolle@ensta-bretagne.org
(L. Lapostolle), leo.morin@ensam.eu (L. Morin), katell.derrien@ensam.eu
(K. Derrien), laurent.berthe@cnrs.fr (L. Berthe), olivier@castelnau@ensam.eu
(O. Castelnau)

Abstract. This paper aims at providing exact expressions for the mechanical fields induced by Laser Shock Peening and comparing them to their numerical estimations. We use a uniaxial strain field hypothesis with an elastic perfectly plastic behavior to derive the stress wave equation. An exact solution to this equation is given using the method of characteristics for a step time profile for the pressure loading, and numerically using finite differences schemes adapted for this hyperbolic equation. An additional residual stress modeling is used, providing the residual stress distribution assuming a planar infinite plate with a finite thickness. Results are presented for three loading pressures, each one corresponding to a different structure in the exact solution. The exact and numerical results present a good match, allowing either the use of the exact solution for an initial estimation of the mechanical fields, or to test the accuracy of other numerical methods.

* Corresponding author.

Résumé. Cet article vise à fournir des expressions exactes pour les champs mécaniques induits par le grenaillage laser et à les comparer à leurs estimations numériques. Nous utilisons une hypothèse de champ de déformation uniaxial avec un comportement élastique parfaitement plastique pour obtenir l'équation de l'onde de contrainte. Une solution exacte de cette équation est donnée en utilisant la méthode des caractéristiques pour un profil temporel de la charge de pression, et numériquement en utilisant des schémas de différences finies adaptés à cette équation hyperbolique. Une modélisation supplémentaire des contraintes résiduelles est utilisée, fournissant la distribution des contraintes résiduelles en supposant une plaque infinie plane avec une épaisseur finie. Les résultats sont présentés pour trois pressions de chargement, chacune correspondant à une structure différente dans la solution exacte. Les résultats exacts et numériques présentent une bonne concordance, ce qui permet soit d'utiliser la solution exacte pour une estimation initiale des champs mécaniques, soit de tester la précision d'autres méthodes numériques.

Keywords. Laser shock peening, Elastic-plastic wave propagation, Numerical simulation, Analytical solution, Plastic strains, Residual stresses.

Mots-clés. Grenaillage laser, Propagation d'ondes élasto-plastiques, Simulation numérique, Solution analytique, Déformations plastiques, Contraintes résiduelles.

Funding. Carnot Institute ARTS, French Agence Nationale de la Recherche (ANR), research project ForgeLaser (Grant agreement no. ANR-18-CE08-0026).

Manuscript received 24 April 2023, revised 2 August 2023 and 18 September 2023, accepted 18 September 2023.

1. Introduction

This work tackles aspects of the modeling of the Laser Shock Peening (LSP) process. For this process, a high-energy laser is used to impact the surface of a specimen in order to introduce compressive residual stresses, eventually improving its fatigue behavior. The energy used (~ 10 J) is applied on a laser spot with a diameter of a few millimeters, with an impulsion of a dozen of nanoseconds, leading to high power densities at the surface (~ 10 GW·cm⁻²) and pressure (a few GPa). These pressures are enough to induce heterogeneous plastic strain fields in the target, leading to residual stresses. Their compressive nature have been related to improved fatigue performances [1,2].

Efforts have been made to model LSP for more than 30 years, starting with the works of Ballard [3] (see also [4]) and Braisted [5] who pioneered the modeling and simulation of LSP. Since then, numerous works were done to evaluate the effects of the different parameters of LSP including size and shape of the laser spot, pressure amplitude, pulse duration, overlapping, etc. [6–10] using finite elements modeling. The effect of the sample microstructure on the wave propagation and the residual stress field has been investigated for 1D laminate specimens [11] and 2D polycrystalline aggregates [12], and a numerical method for fast residual stress estimation has been proposed recently using an elasto-viscoplastic relation [13].

Beside the numerical simulations of LSP, an important aspect of the work of Ballard [3] is to provide an exact solution for the stress wave propagation under certain hypotheses. Indeed, this work shows that for a uniaxial state of strain and an elastic perfectly plastic material, it is possible to predict the stress and velocity wave caused by a pressure step loading. Exact solutions are particularly useful, because they can notably provide a baseline to assess the quality of a numerical method. This was exploited by Heuzé [14] who considers the case of a finite impact (i.e. a loading with a given duration after which it becomes zero), but using a bar modeling, i.e. a single non vanishing stress component (see also [15]), which provides different results than with a uniaxial strain modeling, as considered here and better suited for modelling the mechanical fields at the center of the LSP impact. The structure of the exact solution in the uniaxial strain case is introduced in the work of Wang [16] for a specific range of pressure amplitudes leading to complex interaction between elastic and plastic waves. In addition, semi-analytical solutions also exist for the residual stress profile, based on a heterogeneous eigenstrain distribution. The eigenstrain incompatibilities caused by this distribution generate elastic strains for the structure

to be at equilibrium, leading to residual stresses. Such an approach was already widely used in the literature [13, 17–20], and particularly in the case of Almen strips deflection analysis [21].

Several numerical methods can be used to simulate LSP. The most widely used method is the finite elements method (see for example [5, 7, 10]). However other methods can be used for the problem of a stress wave propagation, using notably a finite differences approach [14, 22, 23]. The numerical procedures of these methods do not concern the same formulation, and the wave equation with the displacement field as unknown used in finite element solvers can be recast as a set of conservation laws on the stress and velocity fields, for which finite-differences based numerical methods can be used.

The aim of this work is to extend the work of Ballard [3], as well as reporting some aspects of the exact solutions that were previously overlooked or not investigated. In particular, we provide a detailed exact solution for the elasto-plastic uniaxial stress/velocity wave and the various reflection phenomenon caused by plasticity, but also for the plastic strain distribution caused by the propagation, which has not been previously reported in such detail. We use these results to give an in-depth exact solution for the residual stress profile, and an exact expression of the surface displacement caused by the laser shock. Such an exact solution dedicated to laser shock applications can be used to provide an initial sensitivity study of some laser parameters, and thus helps optimize the number of experiments needed to observe specific behaviors. Moreover, by comparing the exact solution to the various numerical methods, we also provide some insights as to which ones are better suited to tackle this problem. The article is organized as follows: Section 2 details the mechanical modeling of the problem, the stress wave equation and its exact and numerical solutions. Section 3 presents the residual stresses modeling and the underlying hypotheses. Section 4 presents results, both exact and numerical, for two loading amplitudes, each leading to a different exact solution. Finally, Section 5 discusses the results, provides some additional information for their interpretation and further clarifies the position of the current work with respect to the cited literature in light of the presented results.

2. Mechanical modeling of the stress wave propagation

We are concerned with the propagation of elastic-plastic waves produced by a laser shock. An illustration of the problem considered is represented in Figure 1.

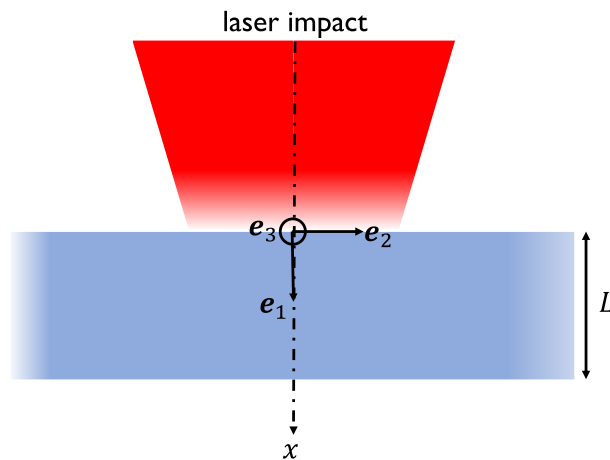


Figure 1. Illustration of the problem.

2.1. Elasto-plastic stress wave equation

2.1.1. Material behavior

The problem of the elasto-plastic shockwave propagation in small strains can be modeled using the following set of equations:

$$\left\{ \begin{array}{ll} \operatorname{div}(\boldsymbol{\sigma}) = \rho \frac{\partial^2 \mathbf{u}}{\partial t^2} & \text{Dynamic equilibrium} \\ \boldsymbol{\sigma} = \mathbb{C} : \boldsymbol{\varepsilon}_e = \mathbb{C} : (\boldsymbol{\varepsilon} - \boldsymbol{\varepsilon}_p) & \text{Elastic behavior} \\ \boldsymbol{\varepsilon} = \frac{1}{2} (\nabla \mathbf{u} + \nabla^T \mathbf{u}) & \text{Strain-displacement relation} \\ f = \sigma_{\text{vM}}(\boldsymbol{\sigma} - \mathbf{X}) - R(p) \leq 0 & \text{Plasticity criterion} \\ \left\{ \begin{array}{l} \dot{\boldsymbol{\varepsilon}}_p = \dot{\lambda} \frac{\partial f}{\partial \boldsymbol{\sigma}} \\ \dot{\lambda} \geq 0 \\ \dot{\lambda} f = 0 \end{array} \right. & \text{Flow rule and consistency conditions} \\ \left\{ \begin{array}{l} \sigma_{11}(x=0, t) = -P(H(t) - H(t - t_0)) \quad \forall t \\ \sigma_{11}(x=L, t) = 0 \quad \forall t \\ \sigma_{11}(x, t=0) = 0 \quad \forall x. \end{array} \right. & \text{Boundary and initial conditions} \end{array} \right. \quad (1)$$

In Equation (1), $\boldsymbol{\sigma}$ is the Cauchy stress tensor, \mathbf{u} the displacement field, $\boldsymbol{\varepsilon}$ the total strain tensor, $\boldsymbol{\varepsilon}_e$ the elastic strain tensor and $\boldsymbol{\varepsilon}_p$ the plastic strain tensor. The material properties are the stiffness tensor \mathbb{C} and the density ρ . f denotes the plasticity criterion, in which \mathbf{X} is the backstress used for kinematic hardening, R the isotropic hardening function, p the accumulated plastic strain and $\dot{\lambda}$ the plastic multiplier. σ_{vM} is the von Mises equivalent stress, defined using J_2 , the second stress tensor invariant:

$$\sigma_{\text{vM}} = \sqrt{3J_2} \quad \text{and} \quad J_2(\boldsymbol{\sigma}) = \frac{1}{2} \boldsymbol{\sigma}_d : \boldsymbol{\sigma}_d, \quad (2)$$

where $\boldsymbol{\sigma}_d$ is the deviatoric part of the stress tensor defined as $\boldsymbol{\sigma}_d = \boldsymbol{\sigma} - (1/3)\operatorname{Tr}(\boldsymbol{\sigma})\mathbf{I}$, \mathbf{I} being the second-order identity tensor. The $\operatorname{Tr}(\cdot)$ notation corresponds to the Trace operator. In the boundary conditions of Equation (1)₆, the H function is the Heaviside step function, P the strictly positive plasma pressure, and t_0 a strictly positive impulsion time. The material is at rest initially, and not previously loaded, so that $\mathbf{v}(x, t=0) = \mathbf{0}$, $\mathbf{u}(x, t=0) = \mathbf{0}$ ($\mathbf{v} = \partial \mathbf{u} / \partial t$) and $\boldsymbol{\varepsilon}_p(x, t=0) = \mathbf{0}$, for all x .

Thereafter, we consider the following hypotheses. Following several works [3, 11, 13, 14] and with in mind the derivation of an exact solution, we assume a uniaxial total strain field, such that

$$\boldsymbol{\varepsilon} = \varepsilon_{11}(x, t) \mathbf{e}_1 \otimes \mathbf{e}_1, \quad (3)$$

\mathbf{e}_1 being a unit vector in the direction of the propagation. Experimentally, such a situation may be reached when the diameter of the laser spot is much greater than the specimen thickness [13, 24]. In this paper, we consider a LSP-type situation, where L is very large (a few cm, as opposed to the thickness of specimens used for backface velocity VISAR measurements which are thin [24, 25]). We also make the (standard) hypothesis of incompressible plasticity, so that we have

$$\boldsymbol{\varepsilon}_p = \varepsilon_p(x, t) \left(\mathbf{e}_1 \otimes \mathbf{e}_1 - \frac{1}{2} \mathbf{e}_2 \otimes \mathbf{e}_2 - \frac{1}{2} \mathbf{e}_3 \otimes \mathbf{e}_3 \right). \quad (4)$$

For simplicity, the developments will be made in the case of homogeneous isotropic material (even though they could be extended to more complex material symmetries). Thus, the stiffness tensor is expressed by:

$$\mathbb{C} = 2\mu \mathbb{K} + 3\kappa \mathbb{J}, \quad (5)$$

with

$$\mathbb{J} = \frac{1}{3} \mathbf{I} \otimes \mathbf{I} \quad \text{and} \quad \mathbb{K} = \mathbb{I} - \mathbb{J}, \quad (6)$$

\mathbb{I} being the fourth-order identity tensor. In Equation (5), μ is the shear modulus and κ the bulk modulus. In these conditions, the stress tensor takes the following form:

$$\boldsymbol{\sigma} = \sigma_{11}(x, t) \mathbf{e}_1 \otimes \mathbf{e}_1 + \sigma_{22}(\mathbf{e}_2 \otimes \mathbf{e}_2 + \mathbf{e}_3 \otimes \mathbf{e}_3). \quad (7)$$

Finally, we consider the case of an elastic perfectly plastic behavior, i.e. with no kinematic nor isotropic hardening: $\mathbf{X} = \mathbf{0}$ and $R(p) = \sigma_y$, σ_y being the yield strength of the material. The plasticity criterion of Equation (1)₄ reduces to:

$$f = |\sigma_{11} - \sigma_{22}| - \sigma_y. \quad (8)$$

It can be noted that in this case, the Tresca and von Mises yield criteria adopt the same expression, given in Equation (8). As pointed out by Heuzé [14], it is useful to rewrite Equation (8) in the following form:

$$f = \left| \frac{6\mu}{3\kappa + 4\mu} \sigma_{11} - \frac{9\kappa\mu}{3\kappa + 4\mu} \varepsilon_p \right| - \sigma_y. \quad (9)$$

Notably, Equation (9) allows the determination of the axial stress value corresponding to the onset of plasticity in a material with no residual plastic strain:

$$\sigma_{\text{hel}} = \left(\frac{2}{3} + \frac{\kappa}{2\mu} \right) \sigma_y, \quad (10)$$

where σ_{hel} is called the Hugoniot Elastic Limit (HEL).

2.1.2. Stress wave equation

We derive here the stress wave propagation equation, which we put in the form of a hyperbolic system, following the same developments as in previous works [11, 13, 14]. Equation (1)₁ combined with Equation (1)₂ derived with respect to time yields the following system:

$$\begin{cases} \frac{\partial \sigma_{11}}{\partial x} = \rho \frac{\partial^2 u_1}{\partial t^2} = \rho \frac{\partial v_1}{\partial t} \\ \frac{\partial \sigma_{11}}{\partial t} = \left(\kappa + \frac{4}{3}\mu \right) \frac{\partial \varepsilon_{11}}{\partial t} - 2\mu \frac{\partial \varepsilon_p}{\partial t}, \end{cases} \quad (11)$$

where v_1 is the axial velocity component. Under a small strain hypothesis, we can write

$$\frac{\partial \varepsilon_{11}}{\partial t} = \frac{\partial}{\partial t} \left(\frac{\partial u_1}{\partial x} \right) = \frac{\partial}{\partial x} \left(\frac{\partial u_1}{\partial t} \right) = \frac{\partial v_1}{\partial x}. \quad (12)$$

Thus the system of Equation (11) can be rewritten as

$$\begin{cases} \frac{\partial \sigma_{11}}{\partial x} = \rho \frac{\partial v_1}{\partial t} \\ \frac{\partial \sigma_{11}}{\partial t} = \left(\kappa + \frac{4}{3}\mu \right) \frac{\partial v_1}{\partial x} - 2\mu \frac{\partial \varepsilon_p}{\partial t}. \end{cases} \quad (13)$$

Firstly we consider the case of a purely elastic propagation, i.e. $\partial \varepsilon_p / \partial t = 0$, Equation (13) thus becomes

$$\frac{\partial \mathbf{U}}{\partial t} + \mathbf{A}_{\text{el}} \frac{\partial \mathbf{U}}{\partial x} = \mathbf{0}, \quad (14)$$

where

$$\mathbf{U} = \begin{pmatrix} \sigma_{11} \\ \nu_1 \end{pmatrix} \quad \text{and} \quad \mathbf{A}_{\text{el}} = \begin{pmatrix} 0 & -\left(\kappa + \frac{4}{3}\mu\right) \\ -\frac{1}{\rho} & 0 \end{pmatrix}. \quad (15)$$

Equation (14) is the so-called advection equation, and can be solved analytically and using dedicated numerical schemes to compute the elastic stress wave propagation.

We consider then the case where the propagation is elasto-plastic, i.e. $\partial \varepsilon_p / \partial t \neq 0$. Here, by taking the time derivative of the plasticity criterion (Equation (1)₄), and expressing the stress components using the elastic behavior (Equation (1)₂), we obtain the following relation:

$$\frac{\partial \varepsilon_p}{\partial t} = \frac{2}{3} \frac{\partial \varepsilon_{11}}{\partial t}. \quad (16)$$

By injecting Equation (16) into Equation (13), we obtain:

$$\frac{\partial \mathbf{U}}{\partial t} + \mathbf{A}_{\text{pl}} \frac{\partial \mathbf{U}}{\partial x} = \mathbf{0}, \quad (17)$$

where the matrix \mathbf{A}_{pl} reads

$$\mathbf{A}_{\text{pl}} = \begin{pmatrix} 0 & -\kappa \\ -\frac{1}{\rho} & 0 \end{pmatrix}. \quad (18)$$

It can be noted that the eigenvalues (in absolute value) of matrices \mathbf{A}_{el} and \mathbf{A}_{pl} provide the stress wave velocities when the wave is elastic, noted c_{el} and when the wave is plastic, noted c_{pl} :

$$c_{\text{el}} = \sqrt{\frac{\kappa + \frac{4}{3}\mu}{\rho}} \quad \text{and} \quad c_{\text{pl}} = \sqrt{\frac{\kappa}{\rho}}. \quad (19)$$

We thus have $c_{\text{el}} > c_{\text{pl}}$, which means that a stress wave loses speed when it induces plastic strains. Finally, the displacement field can be recovered with:

$$u_1(x, t) = \int_{t=0}^t v(x, t) dt + u_1(x, t=0). \quad (20)$$

This quantity is interesting because the displacement of the front face after the shock (i.e. at large t) can be experimentally measured by profilometry [9, 26–28].

In summary, Equation (14) is solved as an elastic predictor step at each time increment. If the stress state complies with the yield condition, then it is adopted as the final state, and the simulation goes on to the next time increment. If not, then Equation (17) is solved, and the solution replaces the one computed with the elastic predictor step. The fields of σ_{22} and ε_p can be recovered by using Equation (8), and Equations (1)₂ and (16) respectively.

2.2. Exact solution

Equations (14) and (17) are hyperbolic systems, and they can be solved analytically, using the methods of characteristics, whose description can be found in several works [3, 14, 15, 22]. The solution \mathbf{U} of the advection equation is constant along lines in the (x, t) plane called characteristic lines, defined by the following equations:

$$\begin{cases} dx = \pm c dt & \text{characteristic line equation} \\ \llbracket \sigma \rrbracket = \mp \rho c \llbracket v \rrbracket & \text{momentum conservation condition,} \end{cases} \quad (21)$$

where c is a generic notation for the stress wave velocity, whether it is elastic or plastic. From Equation (21)₁, we deduce the general equation for the characteristic lines: $t = x/c + t_0$. These lines delimitate zones in the (x, t) plane in which \mathbf{U} , and thus σ_{11} and ν_1 , are constant. There

are as many characteristic lines as there are wave fronts, whether they are loading or unloading the material, or propagating following \mathbf{e}_1 or along the reversed direction. Equation (21)₁, by convention, is written with a “+” sign when the wave is propagating following \mathbf{e}_1 , and with a “−” sign in the opposite direction. Equation (21)₂ gives a relation between the stress and velocity variations from one side of the wave front to the other [15]. The notation $\llbracket \cdot \rrbracket$ corresponds to the difference of a given quantity between each side of the wave front. Thus, knowing the stress values from either sides of a wave front, and one value of velocity, one can deduce the values of velocities at all instants of the propagation. Here, following [15, 16], Equation (21)₂ is used with a “−” sign when the wave is propagating following \mathbf{e}_1 , but the opposite sign must be applied when it is propagating in the opposite direction. One can thus use these relations to plot a so-called x – t diagram, displaying the various characteristic lines, which can be used to compute the stress and velocity states for any given time or location.

2.3. Numerical implementation of the stress wave equation

We present here the numerical implementation of the stress wave equation. As a hyperbolic system, the stress wave equation can be solved using an explicit finite differences approach based on several numerical schemes. We follow the methodology of Leveque [22], and introduce the space and time increments, Δx and Δt respectively, such that $x_{i+1} = x_i + \Delta x$ and $t^{n+1} = t^n + \Delta t$. The notation $(\cdot)_i$ refers to quantities evaluated at $x = x_i$, and $(\cdot)^n$ at $t = t^n$. The explicit procedures that can be used for this problem must however abide the so-called Courant–Friedrichs–Lewy (CFL) condition:

$$\text{CFL} = c_{\text{el}} \frac{\Delta t}{\Delta x} \leq 1, \quad (22)$$

which implies that the lower Δx is, the lower Δt must be for the CFL condition to be verified, which increases the number of steps of the simulation. The elastic velocity is used in Equation (22) so that the CFL condition is valid even when the wave is propagating at speed c_{pl} . The numerical solution of Equations (14) and (17) has the following form:

$$\mathbf{U}_i^{n+1} = \mathbf{U}_i^n - \frac{\Delta t}{\Delta x} (\mathbf{F}_{i+1/2}^n - \mathbf{F}_{i-1/2}^n). \quad (23)$$

The quantity \mathbf{F} is called a flux, and its expression depends on the chosen numerical scheme. In this work we will compare several schemes, namely the Lax–Friedrichs (LF), Lax–Wendroff (LW), Godunov and Godunov with High Resolution (GHR) schemes. Because of their different expressions, these schemes introduce various degrees of artificial viscosity or oscillations. As an example, the GHR scheme actively tries to limit these phenomenon by adding or reducing the artificial viscosity when the rates of the unknowns are high or low. A comprehensive description of these schemes can be found in Leveque [22] and a short summary is provided in Appendix B. Additionally, this problem can be solved using a finite element approach (and in particular the commercial software ABAQUS). In this case, an axisymmetric model is used with a standard/explicit procedure, and with the pressure applied over a very large spot (radius 1 cm) so as to mimic a uniaxial case. In 3D, stress wave edge effects originate from the edges of the laser spot and propagate inward, eventually introducing a perturbation at the center of the impact [24, 29]. However the larger the spot size, the longer this perturbation takes to arrive at the center, which is where the analytical expressions are valid.

For all the numerical schemes, the expression of \mathbf{F} depends on matrices \mathbf{A}_{el} or \mathbf{A}_{pl} of Equations (14) and (17) depending on the elastic or plastic nature of the propagation. The numerical resolution will thus adopt the following strategy: a predictor step will be computed by solving Equation (14). In the case of the GHR scheme, the flux limiter (see Equation (B52)) is also applied

to plastic waves during the correction. Then the plasticity criterion will be checked, and Equation (17) will be solved at the points where the predictor steps violates the plasticity criterion. At those points, the increment of plastic strain can be computed by using Equation (16) in Equation (11)₂:

$$\Delta \varepsilon_p = \frac{2\Delta \sigma_{11}}{3\kappa}, \quad (24)$$

with $\Delta \sigma_{11}$ known from the resolution of the advection equation. We specify that the notation $\Delta(\cdot)$ applied to σ_{11} or ε_p refers to a time increment: $\Delta \sigma_{11} = \sigma_{11}^{n+1} - \sigma_{11}^n$. This approach has the advantage of preserving numerical accuracy during the plastic correction, since the same numerical method is used. Another possible approach would be to compute the plastic correction not with the stress wave equation but with a radial return procedure (see for instance [13]). Both approaches are almost equivalent as shown in Appendix A of Lapostolle [30]. Using a radial return procedure was found to increase the numerical viscosity while avoiding plastic strain overshoot at the boundary.

3. Residual stresses modeling

In this section we detail the hypotheses for the residual stresses modeling, following several works of the literature [13, 17–20, 31]. The modeling assumes a finite plate of thickness L with infinite dimensions in the plane directions, with a heterogeneous plastic strain field along the thickness. The plate is allowed to bend. This plastic strain field corresponds to the one computed by the propagation of the stress wave in Section 2, which is axisymmetric and only varies in the \mathbf{e}_1 direction. The total strain field is also axisymmetric and has the following expression:

$$\boldsymbol{\varepsilon}(x) = \varepsilon_{11}(x)\mathbf{e}_1 + \varepsilon_{22}(x)(\mathbf{e}_2 \otimes \mathbf{e}_2 + \mathbf{e}_3 \otimes \mathbf{e}_3). \quad (25)$$

The resolution of the compatibility equations imposes the form of the radial strain components:

$$\varepsilon_{22}(x) = \varepsilon_{33}(x) = \alpha x + \beta, \quad (26)$$

where α and β are constants to be computed so that the residual stresses are at equilibrium along the thickness in the absence of external forces. Because the gradient of the mechanical fields is only non zero in the \mathbf{e}_1 direction, and since the axial stress is 0 at the surface, the static equilibrium yields

$$\sigma_{11}(x) = 0 \quad \forall x. \quad (27)$$

Using Hooke's law Equation (1)₂ with Equations (25), (4) and (27), we have

$$\sigma_{22}(x) = \sigma_{33}(x) = \frac{18\kappa\mu}{3\kappa + 4\mu} \left(\alpha x + \beta + \frac{\varepsilon_p(x)}{2} \right). \quad (28)$$

The conditions to compute the constants α and β of Equation (26) are the enforcement of zero normal force and bending moment:

$$\begin{cases} \int_0^L \sigma_{22}(x) dx = 0 & \text{normal force} \\ \int_0^L \sigma_{22}(x) x dx = 0 & \text{bending moment,} \end{cases} \quad (29)$$

leading to

$$\begin{cases} L\left(\frac{\alpha L}{2} + \beta\right) = -\int_0^L \frac{\varepsilon_p(x)}{2} dx = \Gamma_1 \\ L^2\left(\frac{\alpha L}{3} + \frac{\beta}{2}\right) = -\int_0^L \frac{\varepsilon_p(x)}{2} x dx = \Gamma_2, \end{cases} \quad (30)$$

which resolution leads to

$$\begin{cases} \alpha = \frac{12}{L^3} \left(\Gamma_2 - \frac{L\Gamma_1}{2} \right) \\ \beta = \frac{2}{L} \left(2\Gamma_1 - \frac{3\Gamma_2}{L} \right). \end{cases} \quad (31)$$

Knowing the distribution of $\varepsilon_p(x)$ from the propagation simulation, one is thus able to compute the residual stresses using Equation (28). It is also possible to compute the curvature radius of the plate [17]:

$$R = \frac{L^3}{6(2\Gamma_2 - L\Gamma_1)}. \quad (32)$$

As we will see with the results of Section 4, the plastic strain field has step-wise constant in-depth profile, which will allow a fully analytical expression of Γ_1 and Γ_2 of Equation (30), and thus of the residual stresses.

4. Results

In this section, we present results for the stress wave propagation, both analytically and numerically. We distinguish three cases: $P \leq \sigma_{\text{hel}}$, $\sigma_{\text{hel}} < P \leq 2\sigma_{\text{hel}}$ and $P > (c_e + 5c_p)/(c_e + c_p)\sigma_{\text{hel}} > 2\sigma_{\text{hel}}$, P being the positive plasma pressure. The intermediary subcase of $P > 2\sigma_{\text{hel}}$, namely $2\sigma_{\text{hel}} < P \leq (c_e + 5c_p)/(c_e + c_p)\sigma_{\text{hel}}$ is detailed below. Indeed when a material is loaded such that $\sigma_{11} = -P < -\sigma_{\text{hel}}$, the induced plastic strain is

$$\varepsilon_p = -\frac{2}{3} \frac{P - \sigma_{\text{hel}}}{\kappa}, \quad (33)$$

according to the plasticity criterion of Equation (9). The value of axial stress inducing plastic strain during the unloading, given the already induced plastic strain, is $P - 2\sigma_{\text{hel}}$. Given that the value of the axial stress cannot change sign during the unloading, then no plastic strains are induced during the unloading if $P \leq 2\sigma_{\text{hel}}$. On the contrary, plastic strain will be induced during the unloading if $P > 2\sigma_{\text{hel}}$. A subcase of this last condition is $2\sigma_{\text{hel}} < P \leq (c_e + 5c_p)/(c_e + c_p)\sigma_{\text{hel}}$, whose exact solution structure is presented in Wang [16]. The main difference is that though plastic strains are induced during the unloading in both subcases (same exact solution in the initial instants), the case with $P > (c_e + 5c_p)/(c_e + c_p)\sigma_{\text{hel}}$ induces plastic strains over a greater depth, changing the subsequent layout of the exact solution compared to the other subcase, since it gives rise to different wave interactions. See Figure 7 for more details.

In the following, we consider a steel-like material with $\kappa = 175$ GPa, $\mu = 80.8$ GPa, $\rho = 7800$ kg·m⁻³, and with a yield strength of $\sigma_y = 870$ MPa, leading to $\sigma_{\text{hel}} = 1522.5$ MPa. The loading remains a step function of amplitude $-P$ and of duration $t_0 = 80$ ns. The boundary conditions are specified in Equation (1)₆. For the whole section, numerical results will be presented, using the following parameters: the length of the domain is $L = 14$ mm, the duration of the simulation is $T = 800$ ns, the spatial increment is $\Delta x = 3.5$ μ m, and the CFL number is 0.95.

Hereafter, in order to shorten the notations, the axial stress component σ_{11} will be simply noted σ , and the axial velocity component v_1 simply v .

4.1. Case 1: $P \leq \sigma_{\text{hel}}$

This trivial case of pure elastic response allows to illustrate the x - t diagram for a simple solution. The corresponding x - t diagram is presented in Figure 2, in which two parallel characteristics lines are plotted, one for loading front of the wave, the other for the unloading front, the latter being shifted by t_0 .

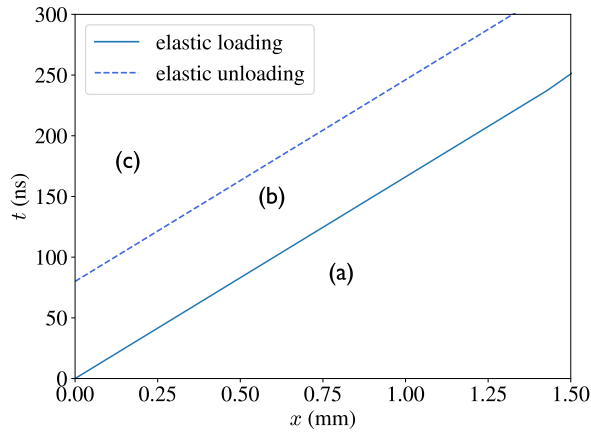


Figure 2. x - t diagram in the case of a purely elastic propagation. The letters identify areas in the diagram.

For each zones of the x - t diagram of Figure 2, it is straightforward to attribute an axial stress value. Using the compatibility equation of Equation (21)₂, one can then compute the velocity values of the x - t diagram. Their expressions are given in Table 1.

Table 1. Values of axial stress and velocities of the x - t diagram of Figure 2

Zone i of the x - t diagram	σ_i	v_i
a	0	0
b	$-P$	$\frac{P}{\rho c_e}$
c	0	0

As no plastic deformation occurs in this case, no residual stress is generated by the shock wave. This methodology will be applied to the more complex wave propagations, where plastic strain is induced.

4.2. Case 2: $\sigma_{\text{hel}} < P \leq 2\sigma_{\text{hel}}$

We now consider the case where $\sigma_{\text{hel}} < P \leq 2\sigma_{\text{hel}}$, with $P = 2$ GPa. Figure 3 presents the corresponding exact x - t diagram, as well a numerical x - t diagram computed using the Godunov High Resolution method presented in Section 2.3.

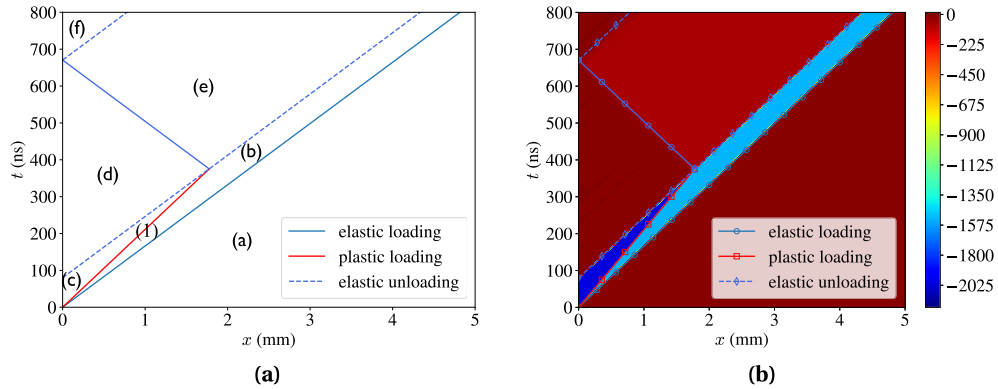


Figure 3. $x-t$ diagrams in the case where $\sigma_{\text{hel}} < P \leq 2\sigma_{\text{hel}}$. (a) Exact $x-t$ diagram. The letters identify areas within the diagram, the number the wave front which induces plasticity. (b) Comparison between the exact and numerical $x-t$ diagrams for the axial stress.

Figure 3(a) presents characteristic lines with different slopes. The red line, identified by the number (1) corresponds to the plastic loading front, which propagates at the speed c_p . Since plastic strain does not occur during the unloading in this case, no characteristic line of slope $1/c_p$ originates at t_0 . The values of stress and velocity for the $x-t$ diagram of Figure 3(a) are summarized in Table 2.

Table 2. Values of axial stress and velocity in the zones of the $x-t$ diagram of Figure 3

Zone i of the $x-t$ diagram	σ_i	v_i
a	0	0
b	$-\sigma_{\text{hel}}$	$\frac{\sigma_{\text{hel}}}{\rho c_e}$
c	$-P$	$\frac{P c_e + \sigma_{\text{hel}}(c_p - c_e)}{\rho c_e c_p}$
d	0	$\frac{(P - \sigma_{\text{hel}})(c_e - c_p)}{\rho c_e c_p}$
e	$\frac{(P - \sigma_{\text{hel}})(c_p - c_e)}{2c_p}$	$\frac{(P - \sigma_{\text{hel}})(c_e - c_p)}{2\rho c_e c_p}$
f	0	0

Table 3 presents the exact value of plastic strain induced by the plastic loading front in the $x-t$ diagram of Figure 3. It can be computed using the plasticity criterion of Equation (1)₄.

Table 3. Values of the axial plastic strain induced by the plastic front of the $x-t$ diagram of Figure 3

Plastic front i of the $x-t$ diagram	$\epsilon_{p,i}$
1	$-\frac{2}{3} \frac{P - \sigma_{\text{hel}}}{\kappa}$

For each of the zones (identified with letters from (a) to (f)) of the $x-t$ diagram of Figure 3, the axial stress and velocity can be computed. During the loading front, the stress in zone (b) reaches the lowest value possible without inducing plasticity, i.e. $-\sigma_{\text{hel}}$. Once plasticity is induced, the stress reaches the prescribed value $-P$ in zone (c), before coming back to 0 once the wave has passed in zone (d). For each of these zones, the velocity can be deduced using Equation (21)₂. Since the elastic and plastic fronts do not propagate at the same speed, the elastic unloading front eventually catches up the plastic loading front. Because of the different speeds, the fronts interact with each other, in the similar way of an interface between two materials with different impedance. Transmitted and reflected waves are created, thus delimiting here zone (e). To compute the values of stress and velocity in this zone, one can take advantage of the loading fronts that zone (e) shares with zones for which the stresses and velocities are already known. In this instance, one must solve the following linear system:

$$\begin{cases} \sigma_{(e)} - \sigma_{(d)} = \rho c_{(e)} (v_{(e)} - v_{(d)}) \\ \sigma_{(e)} - \sigma_{(b)} = -\rho c_{(e)} (v_{(e)} - v_{(b)}). \end{cases} \quad (34)$$

Eventually, the plastic loading front is overtaken by the elastic unloading front, and the stress wave stops inducing plastic strains. At this point, the stress is attenuated (in absolute value) to the highest value of stress that does not generate plastic strains, i.e. σ_{hel} .

We can now use the different values of Tables 2 and 3 with the $x-t$ diagram of Figure 3 to compute analytically the stress, velocity and plastic strain distributions at any given time t . We can see in Figure 3(b) that the numerical solution corresponds very well to the exact $x-t$ diagram, as zones of different stress values are clearly identifiable and delimited by the characteristic lines. These numerical results obtained using various numerical schemes can be compared to the exact solution, which is presented in Figure 4.

The results of Figure 4 show that all numerical methods used are in a globally good agreement with the exact solution, either for the stress, velocity or plastic strain. It must be noted that, for the sake of visibility, the points in the plots of Figure 4 do not correspond to each node, but rather a fixed interval of nodes. This also applies for future figures. Each scheme however has different numerical properties, which can be observed. For instance, the Lax–Wendroff scheme, though precise, introduce some small amounts of artificial oscillations, which can be observed after the unloading front in the stress and velocity profiles. The Lax–Friedrichs scheme is characterized by a large amount of artificial viscosity, which can clearly be seen in the plastic strain profile of Figure 4(f). In all instances, the Godunov with High Resolution scheme proves to be the most precise, as it follows the more closely the exact solution. A quantification of the errors of the schemes with respect to the exact solution will be discussed in Section 5. For the plastic strain, the first points ($x \simeq 0$ mm) are far from the exact solution. This is caused by a large stress increment at the first cell ($x = 0$) due to the instantaneous nature of the loading. As a result, the computed plastic strains exhibits this locally high values. This behavior was also observed for the finite elements solution in the work of Heuzé [14], and is discussed in more details in Section 5.

The plastic strain profile of Figure 4(f) corresponds to the residual plastic strain field (after propagation) and can thus be used to compute the residual stresses presented in Section 3. Moreover, the value of the induced plastic strain, and the depth along which it is induced are known analytically, which allows the exact expression of the integrals in Equation (30). We thus have:

$$\begin{cases} \alpha = \frac{2c_e c_p t_0 (P - \sigma_{\text{hel}}) (L(c_p - c_e) + c_e c_p t_0)}{L^3 \kappa (c_e - c_p)^2} \\ \beta = \frac{c_e c_p t_0 (P - \sigma_{\text{hel}}) (4L(c_e - c_p) - 3c_e c_p t_0)}{3L^2 \kappa (c_e - c_p)^2}. \end{cases} \quad (35)$$

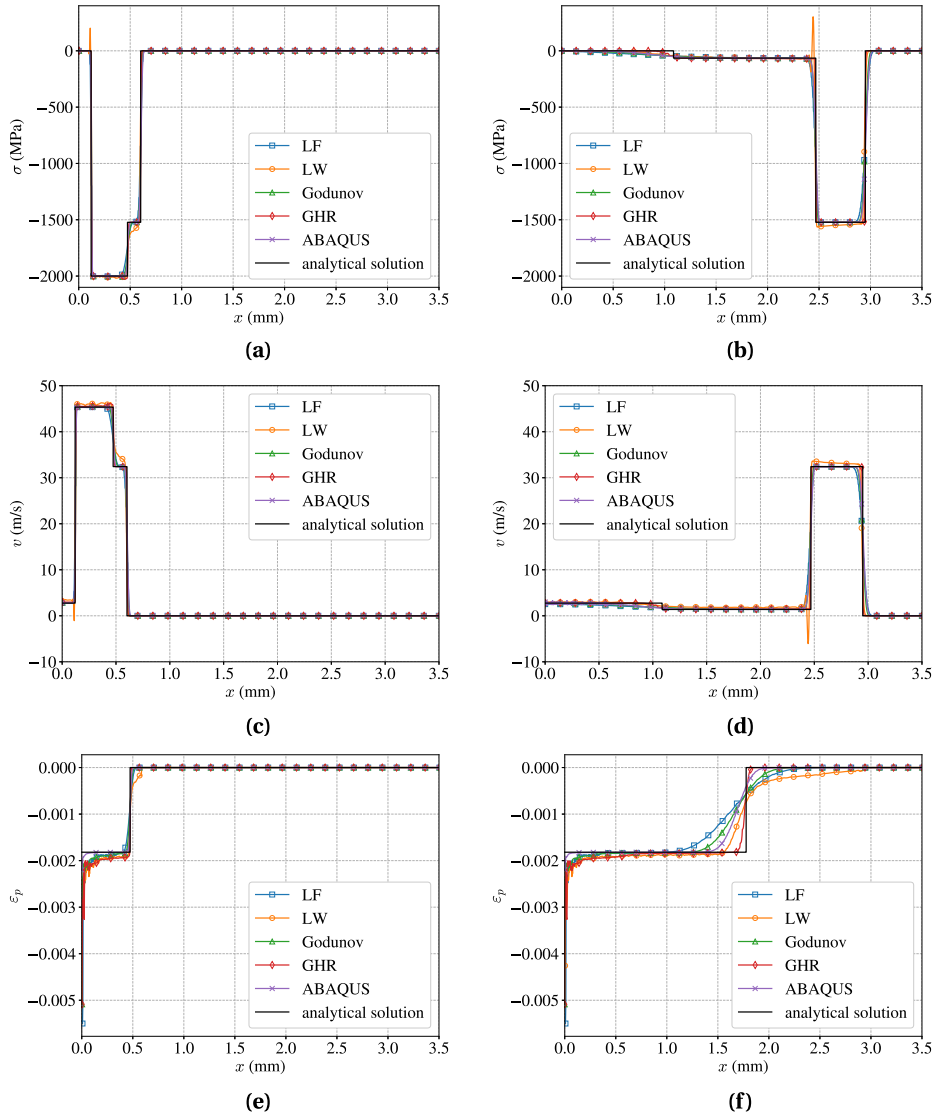


Figure 4. Comparisons of the mechanical fields obtained with the exact solution and with the various numerical methods. (a) Axial stress field at $t = 100$ ns. (b) Axial stress field at $t = 490$ ns. (c) Axial velocity field at $t = 100$ ns. (d) Axial velocity field at $t = 490$ ns. (e) Axial plastic strain field at $t = 100$ ns. (f) Axial plastic strain field at $t = 490$ ns.

The comparison between the exact and numerical residual stresses is presented in Figure 5. For the numerical residual stresses, the integrals of Equation (30) are computed numerically using a trapezoidal rule based of the numerical plastic strain profiles.

The analytical (exact) and numerical residual stress profiles are in very good agreement which is expected since the plastic strain profiles were already close between the different methods. The residual stresses are in compression at the surface, and become in tension further in depth (at $x \approx 1.9$ mm) due to the equilibrium. The surface values of the numerical residual stress profiles are much more in compression than the rest, which is due to the numerical errors at the beginning of the plastic strain profiles.

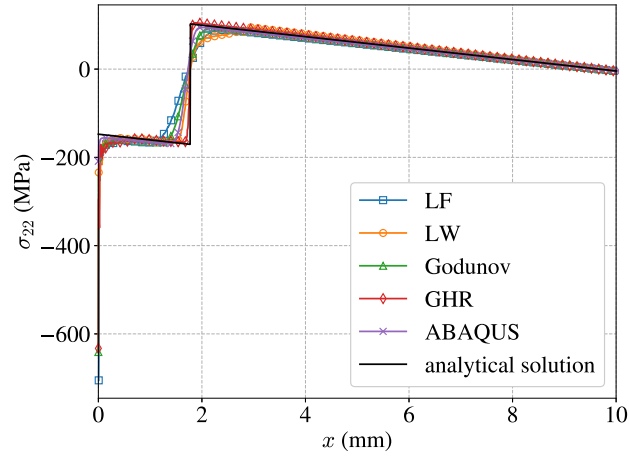


Figure 5. Comparison of the residual stress field obtained with the exact solution and the various numerical methods.

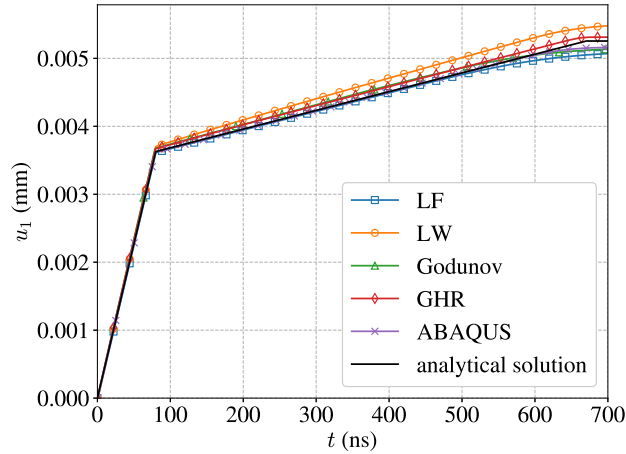


Figure 6. Comparison of the temporal profile of the displacement at the surface of the specimen ($x = 0$) obtained with the exact solution and the various numerical methods.

In a similar manner, we can take advantage of the piece-wise constant nature of the velocity profiles at any given time t to give an exact expression of the displacement field. More precisely, we will take an interest in the surface displacement field, since it can be experimentally measured. To illustrate this, we compute the time evolution of the displacement at the surface of the specimen ($x = 0$) using Equation (20) with the exact solution and the numerical methods. This is presented in Figure 6. The agreement between the exact solution and the numerical methods is relatively good, with some errors introduced by the differences in the velocity predictions, which lead to slightly different slopes in the displacement profiles. The GHR scheme is the closest to the exact solution.

The final value of the displacement at the surface (i.e. once the stress wave has completely passed) can be computed, and reads:

$$u_{1,\text{final}} = \frac{t_0 (P(c_e + 2c_p) - \sigma_{\text{hel}}(c_e + c_p))}{\rho c_e c_p}. \quad (36)$$

4.3. Case 3: $P > (c_e + 5c_p)/(c_e + c_p)\sigma_{\text{hel}}$

We finally consider here the more complex case where the loading amplitude P is such that $P > (c_e + 5c_p)/(c_e + c_p)\sigma_{\text{hel}}$. We use the value of $P = 5$ GPa to illustrate this case. The main particularity in this case is that plastic strains will be induced during the unloading front. This will also create a plastic characteristic line during the unloading, creating more complex interactions between the elastic and plastic parts of the wave. This is illustrated in Figure 7.

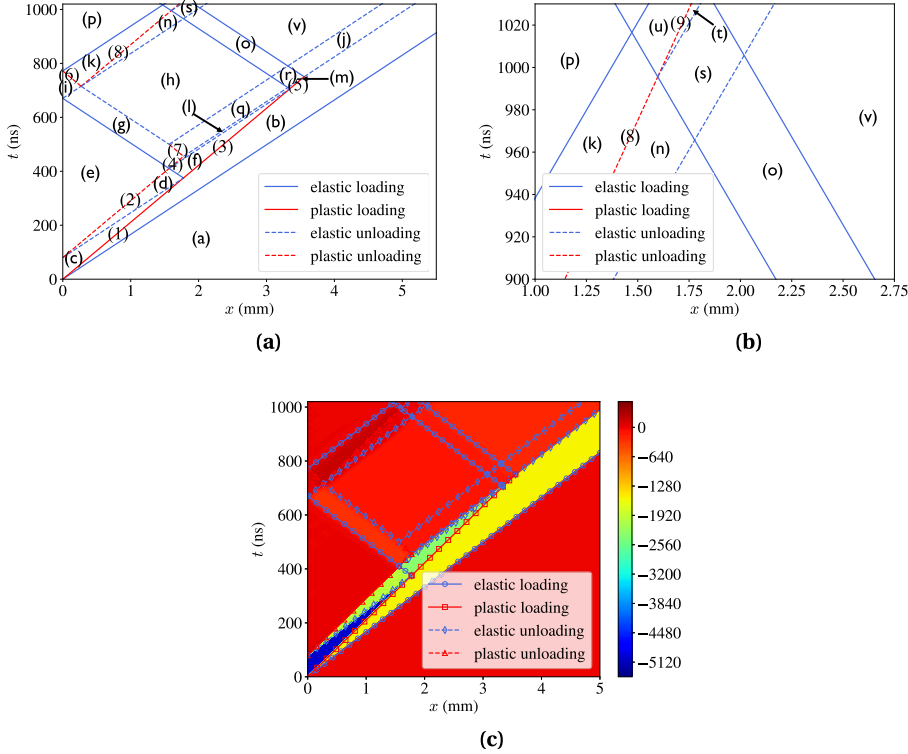


Figure 7. $x-t$ diagrams in the case where $P > (c_e + 5c_p)/(c_e + c_p)\sigma_{\text{hel}}$. (a) Exact $x-t$ diagram. The letters identify areas within the diagram, the number the wave front which induces plasticity. (b) Enlarged view of the $x-t$ diagram. (c) Comparison between the exact and numerical $x-t$ diagrams for the axial stress.

Figure 7(a) presents a much more complex $x-t$ diagram than the one in Figure 3. Notably, a plastic wave front is created during the unloading front. The elastic unloading wave front is thus trapped between two plastic wave fronts of lower velocity, creating a complex pattern of transmitted and reflected wave. The stress and velocity values associated with each zone of Figure 7(a) are summarized in Table 4, and the values of plastic strains induced by the plastic wave fronts in Table 5. These values of stress and velocity are determined either by mechanical analysis (for instance, it is straightforward to associate the stress value of zone b with $-\sigma_{\text{hel}}$ and the one of zone c with $-P$) when possible, or either by solving a linear system similar to Equation (34) when a zone is delimited by two wave fronts that can be exploited.

Table 4. Values of axial stress and velocity in the zones of the $x-t$ diagram of Figure 7

i	σ_i	v_i
a	0	0
b	$-\sigma_{\text{hel}}$	$\frac{\sigma_{\text{hel}}}{\rho c_e}$
c	$-P$	$\frac{P c_e + \sigma_{\text{hel}}(c_p - c_e)}{\rho c_e c_p}$
d	$-P + 2\sigma_{\text{hel}}$	$\frac{P c_e - \sigma_{\text{hel}}(c_e + c_p)}{\rho c_e c_p}$
e	0	$\frac{\sigma_{\text{hel}}(c_e - c_p)}{\rho c_e c_p}$
f	$-\frac{P(c_e + c_p) - 4\sigma_{\text{hel}}c_p}{c_e + c_p}$	$\frac{P c_e(c_e + c_p) + \sigma_{\text{hel}}(c_p^2 - c_e^2 - 4c_e c_p)}{\rho c_e c_p(c_e + c_p)}$
g	$-\frac{4\sigma_{\text{hel}}c_p(c_e - c_p)}{(c_e + c_p)^2}$	$\frac{\sigma_{\text{hel}}(c_e - c_p)^2(c_e + 3c_p)}{\rho c_e c_p(c_e + c_p)^2}$
h	$\frac{(c_e - c_p)(P(c_e + c_p) - 2\sigma_{\text{hel}}(c_e + 3c_p))}{2c_p(c_e + c_p)}$	$\frac{(c_e - c_p)(P(c_e + c_p) - 4\sigma_{\text{hel}}c_p)}{2\rho c_e c_p(c_e + c_p)}$
i	0	$\frac{\sigma_{\text{hel}}(c_e - c_p)(c_e^2 + 2c_e c_p - 7c_p^2)}{\rho c_e c_p(c_e + c_p)^2}$
j	$-\frac{(c_e - c_p)(P(c_e^3 + c_e^2 c_p) - c_e c_p^2 - c_p^3) + \sigma_{\text{hel}}(-c_e^3 - 3c_e^2 c_p + 13c_e^2 c_p - c_p^3)}{2c_p(c_e + c_p)^3}$	$\frac{(c_e - c_p)(P(c_e^3 + c_e^2 c_p - c_e c_p^2 - c_p^3) + \sigma_{\text{hel}}(-c_e^3 - 3c_e^2 c_p + 13c_e^2 c_p - c_p^3))}{2\rho c_e c_p(c_e + c_p)^3}$
k	$\frac{(c_e - c_p)(P(c_e + c_p)^2 + 2\sigma_{\text{hel}}(-c_e^2 - 4c_e c_p + c_p^2))}{2c_e(c_e + c_p)^2}$	$\frac{(c_e - c_p)(P(c_e + c_p)^2 - 4\sigma_{\text{hel}}(c_e c_p + 3c_p^2))}{2\rho c_e c_p(c_e + c_p)^2}$
l	$-P + 2\sigma_{\text{hel}}$	$\frac{P c_e(c_e + c_p) + \sigma_{\text{hel}}(3c_p^2 - c_e^2 - 6c_e c_p)}{\rho c_e c_p(c_e + c_p)}$
m	$-\frac{P(c_e + c_p)^2 - 8\sigma_{\text{hel}}c_e c_p}{(c_e + c_p)^2}$	$\frac{P c_e(c_e + c_p)^2 + \sigma_{\text{hel}}(c_p^3 + c_e^2 c_p - 9c_e^2 c_p - c_p^3)}{\rho c_e c_p(c_e + c_p)^2}$
n	0	$\frac{(c_e - c_p)(P(c_e + c_p) - \sigma_{\text{hel}}(c_e + 5c_p))}{\rho c_e c_p(c_e + c_p)}$
o	$\frac{(c_e - c_p)(P(c_e + c_p)^2 - 2\sigma_{\text{hel}}(c_e^2 + 6c_e c_p + c_p^2))}{2c_p(c_e + c_p)^2}$	$\frac{(c_e - c_p)(P(c_e + c_p)^2 - 8\sigma_{\text{hel}}c_e c_p)}{2\rho c_e c_p(c_e + c_p)^2}$
p	0	$\frac{(c_e - c_p)(P(c_e + c_p)^3 + 2\sigma_{\text{hel}}c_p(-3c_e^2 - 10c_e c_p + c_p^2))}{2\rho c_e^2 c_p(c_e + c_p)^2}$
q	$\frac{(c_e - c_p)(P(c_e + c_p)^2 - 2\sigma_{\text{hel}}(c_e^2 + 6c_e c_p + c_p^2))}{(c_e + c_p)^3}$	$\frac{(c_e - c_p)(P c_e(c_e + c_p)^2 + \sigma_{\text{hel}}(-c_e^3 - 5c_e^2 c_p + c_e c_p^2 - 3c_p^3))}{\rho c_e c_p(c_e + c_p)^3}$
r	$\frac{(c_e - c_p)(P(c_e + c_p)^2 - 4\sigma_{\text{hel}}(c_e^2 + 3c_e c_p))}{(c_e + c_p)^3}$	$\frac{(c_e - c_p)(P c_e(c_e + c_p)^2 + \sigma_{\text{hel}}(-c_e^3 - 7c_e^2 c_p + c_e c_p^2 - c_p^3))}{\rho c_e c_p(c_e + c_p)^3}$
s	$-\frac{2\sigma_{\text{hel}}(c_e - c_p)^2}{(c_e + c_p)^2}$	$\frac{(c_e - c_p)(P(c_e + c_p)^2 - \sigma_{\text{hel}}(c_e^2 + 8c_e c_p + 3c_p^2))}{\rho c_e c_p(c_e + c_p)^2}$
t	0	$\frac{(c_e - c_p)(P(c_e + c_p)^2 - \sigma_{\text{hel}}(c_e^2 + 10c_e c_p + c_p^2))}{\rho c_e c_p(c_e + c_p)^2}$
u	$\frac{(c_e - c_p)(P(c_e + c_p)^3 + 2\sigma_{\text{hel}}(-c_e^3 - 9c_e^2 c_p + c_e c_p^2 + c_p^3))}{2c_e(c_e + c_p)^3}$	$\frac{(c_e - c_p)(P(c_e + c_p)^3 - 4\sigma_{\text{hel}}c_p(c_e^2 + 6c_e c_p + c_p^2))}{2\rho c_e c_p(c_e + c_p)^3}$
v	$-\frac{\sigma_{\text{hel}}(c_e - c_p)}{2c_p}$	$\frac{\sigma_{\text{hel}}(c_e - c_p)}{2\rho c_e c_p}$

In particular, the stress in zone (f) is here high enough to induce plastic strains. This is true only if $\sigma_{(f)} > \sigma_{\text{hel}}$, which yields $P > (c_e + 5c_p)/(c_e + c_p)\sigma_{\text{hel}}$, hence the definition of the loading case considered.¹ The $x-t$ diagram for $2\sigma_{\text{hel}} \leq P < (c_e + 5c_p)/(c_e + c_p)\sigma_{\text{hel}}$ is presented in Wang [16]. In

¹An alternative way to derive this condition is by making the hypothesis of the wave front (3) being elastic, which yields a value of $\sigma_{(f)}$ different from the one in Table 4. However the condition $\sigma_{(f)} < \sigma_{\text{hel}}$ will still lead to the same threshold of $(c_e + 5c_p)/(c_e + c_p)\sigma_{\text{hel}}$.

Table 5. Values of the axial plastic strain induced by the plastic front of the $x-t$ diagram of Figure 7

Plastic front i of the $x-t$ diagram	$\varepsilon_{p,i}$
1	$-\frac{2}{3} \frac{P - \sigma_{\text{hel}}}{\kappa}$
2	$-\frac{2}{3} \frac{\sigma_{\text{hel}}}{\kappa}$
3	$\frac{2(\sigma_{\text{hel}}(c_e + 5c_p) - P(c_e + c_p))}{3\kappa(c_e + c_p)}$
4	$-\frac{2\sigma_{\text{hel}}(c_e^2 + 6c_e c_p - 3c_p^2)}{3\kappa(c_e + c_p)^2}$
5	$-\frac{2(P(c_e + c_p)^2 - \sigma_{\text{hel}}(c_e^2 + c_p^2 + 10c_e c_p))}{3\kappa(c_e + c_p)^2}$
6	$\frac{P(c_e^3 + c_e^2 c_p - c_e c_p^2 - c_p^3) + 2\sigma_{\text{hel}}(-2c_e^3 - 5c_e^2 c_p + 4c_e c_p^2 - c_p^3)}{3\kappa c_e(c_e + c_p)^2}$
7	$2 \frac{P(c_e^3 + c_e^2 c_p - c_e c_p^2 - c_p^3) + \sigma_{\text{hel}}(-3c_e^3 - 13c_e^2 c_p + 7c_e c_p^2 + c_p^3)}{3\kappa(c_e + c_p)^3}$
8	$\frac{P(c_e^3 + c_e^2 c_p - c_e c_p^2 - c_p^3) + 2\sigma_{\text{hel}}(-2c_e^3 - 5c_e^2 c_p + 4c_e c_p^2 - c_p^3)}{3\kappa c_e(c_e + c_p)^2}$
9	$\frac{P(c_e^4 + 2c_e^3 c_p - 2c_e c_p^3 - c_p^4) + 2\sigma_{\text{hel}}(-2c_e^4 - 11c_e^3 c_p + 7c_e^2 c_p^2 - c_e c_p^3 - c_p^4)}{3\kappa c_e(c_e + c_p)^3}$

effect, the results for zones (a) to (e) are the same as the ones presented in Table 4 and fronts (1) and (2) of Table 5, but the subsequent structure of the $x-t$ diagram, and thus of the exact solution, is different.

When compared to the characteristic lines, the numerical results (obtained with the GHR scheme) in Figure 7(b) correspond very well to the stress zones displayed. In Figure 8, we compare results of stress, velocity and plastic strain between the numerical and exact solutions for the various numerical schemes at several time steps.

All the numerical schemes achieve a relatively good approximation of the exact solution, but with more pronounced differences than for the $P = 2$ GPa case. These differences correspond to different degrees of artificial viscosities in the numerical schemes, leading some of them to miss certain fine features of the exact solution. In fact, only the GHR scheme is able to correctly reproduce the smallest variations of stress, velocity and plastic strains (see for instance the last step of plastic strain in Figure 8(f) at $x \approx 3.5$ mm). The other numerical schemes sometimes completely miss the fine features of the exact solution (for instance the part of the stress wave in tension at $x \approx 0.5$ mm in Figure 8(b), which only the LW and GHR schemes reproduce to some degree). Here again, the errors of the scheme with respect to the exact solution are discussed in Section 5.

Similarly to Figure 5, it is possible to compute the residual stresses for the current case. The plastic strain profiles being stepwise constant, it is possible to analytically evaluate the integrals from Equation (30). The resulting coefficients α and β are detailed in Appendix A for the sake of

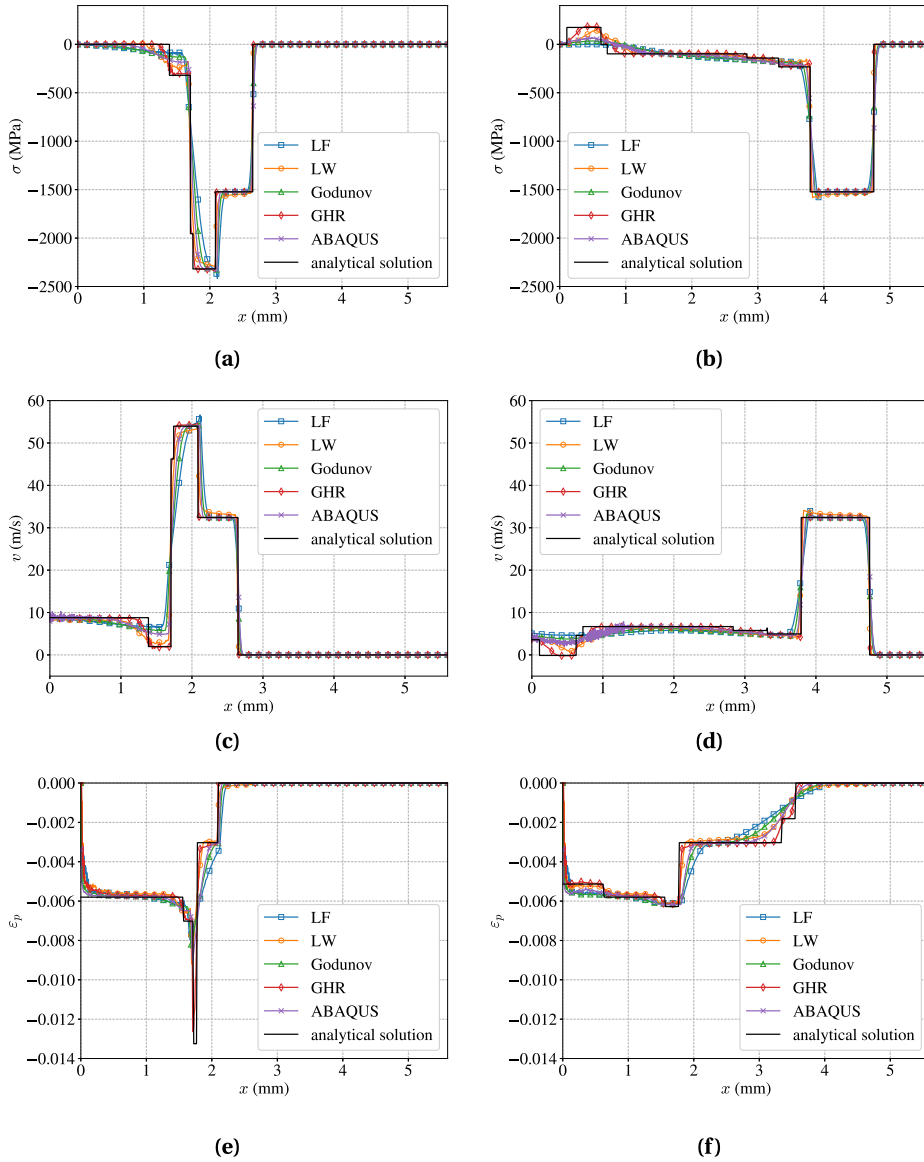


Figure 8. Comparisons of the mechanical fields obtained with the exact solution and with the various numerical methods. (a) Axial stress field at $t = 440$ ns. (b) Axial stress field at $t = 790$ ns. (c) Axial velocity field at $t = 440$ ns. (d) Axial velocity field at $t = 790$ ns. (e) Axial plastic strain field at $t = 440$ ns. (f) Axial plastic strain field at $t = 790$ ns.

conciseness. Figure 9 presents the final plastic strain profile once the stress wave stops inducing them, and the corresponding residual stress profile.

Here again, we can compute the temporal evolution of the displacement of the specimen surface using Equation (20). The results are presented in Figure 10. The agreement between the exact and numerical solution is here again good, the GHR scheme proving the best to approximate the exact solution. Contrary to the profile of Figure 6, the one of Figure 10 presents

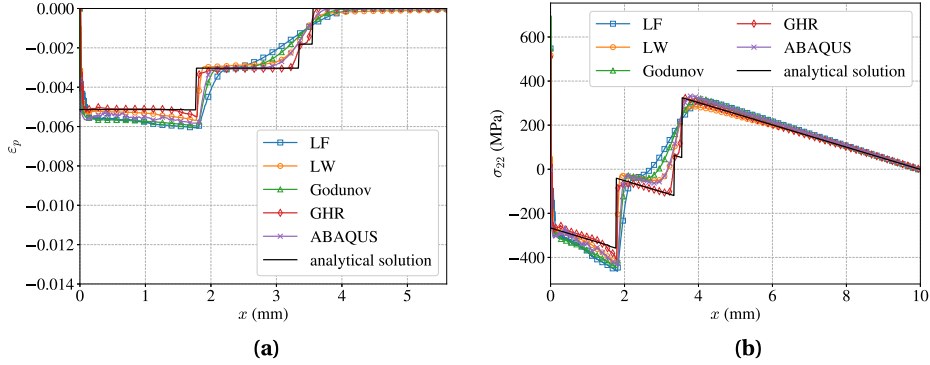


Figure 9. Comparisons of the mechanical fields obtained with the exact solution and with the various numerical methods. (a) Stationary plastic strain field at $t = 1050$ ns. (b) Residual stress field.

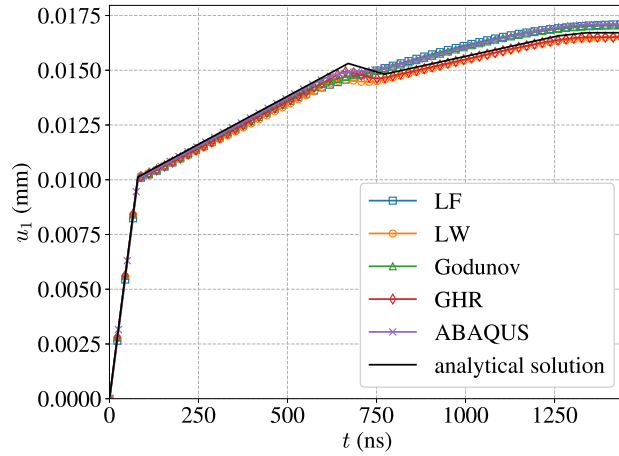


Figure 10. Comparison of the temporal profile of the displacement at the surface of the specimen ($x = 0$) obtained with the exact solution and the various numerical methods.

a decreasing slope at $t \approx 740$ ns. This is due to the secondary wave which has been reflected in tension at the specimen surface (see Figure 8(b) at $x \approx 0.5$ mm).

The exact value of the final displacement of the surface is given in that case by:

$$u_{1,\text{final}} = \frac{-t_0}{2\rho c_e^2 c_p^2 (c_e + c_p)^3} \left(P(c_e^6 - 9c_e^4 c_p^2 - 18c_e^3 c_p^3 - 15c_e^2 c_p^4 - 6c_e c_p^5 - c_p^6) + 2\sigma_{\text{hel}}(-c_e^6 - 4c_e^5 c_p + c_e^4 c_p^2 + 24c_e^3 c_p^3 + c_e^2 c_p^4 + 12c_e c_p^5 - c_p^6) \right). \quad (37)$$

5. Discussion

For both $P = 2$ GPa and $P = 5$ GPa, since $c_e > c_p$, the initial elastic loading front becomes more distant to the plastic loading front, creating the so-called elastic precursor, which is a typical feature of stress wave propagation induced by laser impact. This precursor can be experimentally observed in backface velocity measurements [24, 25, 32].

As a complement to Figures 4 and 8, Table 6 presents the average relative errors between the numerical schemes and analytical expressions. These errors are computed using the profiles at

Table 6. Average relative errors between the exact solutions and the numerical schemes, computed along the length L , at $t = 490$ ns in the case $\sigma_{\text{hel}} < P \leq 2\sigma_{\text{hel}}$ and at $t = 790$ ns in the case $P > (c_e + 5c_p)/(c_e + c_p)\sigma_{\text{hel}}$

	Case $\sigma_{\text{hel}} < P \leq 2\sigma_{\text{hel}}$			Case $P > (c_e + 5c_p)/(c_e + c_p)\sigma_{\text{hel}}$		
	σ	v	ε_p	σ	v	ε_p
Lax–Friedrichs	4.77×10^{-3}	4.86×10^{-3}	2.16×10^{-2}	3.75×10^{-1}	3.77×10^{-1}	2.48×10^{-2}
Lax–Wendroff	3.11×10^{-3}	4.52×10^{-3}	2.09×10^{-2}	3.74×10^{-1}	3.73×10^{-1}	1.42×10^{-2}
Godunov	3.40×10^{-3}	3.41×10^{-3}	1.51×10^{-2}	3.74×10^{-1}	3.74×10^{-1}	1.88×10^{-2}
GHR	8.92×10^{-4}	9.16×10^{-4}	7.93×10^{-3}	3.70×10^{-1}	3.70×10^{-1}	6.41×10^{-3}
ABAQUS	6.52×10^{-3}	6.95×10^{-3}	8.87×10^{-3}	3.66×10^{-1}	3.66×10^{-1}	2.62×10^{-2}

$t = 490$ ns and $t = 790$ ns for the cases $\sigma_{\text{hel}} < P \leq 2\sigma_{\text{hel}}$ and $P > (c_e + 5c_p)/(c_e + c_p)\sigma_{\text{hel}}$ respectively. The relative error is obtained by normalizing the absolute error with the highest value (in absolute value) of each corresponding profile. Table 6 confirms that the GHR scheme is the most precise. Note that, while the errors are of the same order of magnitude, the results from the ABAQUS software give higher errors than the other schemes in most cases.

Most of the exact results presented in this paper are in agreement with work of Ballard [3]. Namely, in the $\sigma_{\text{hel}} < P \leq 2\sigma_{\text{hel}}$ case, the value of the induced plastic strain (see Table 3) linearly depends on the applied pressure P . In the $P > (c_e + 5c_p)/(c_e + c_p)\sigma_{\text{hel}}$ case, the initial plastic loading induces a level of plastic strain that is independent of the applied pressure, and is thus considered as saturated (see line 2 of Table 5). Ballard [3] also presents exact results for the saturated l_{sat} and affected depth l_{plast} . The plastic strain is considered saturated when its value does not depend on the applied pressure, but only on the material parameters (see line 2 of Table 5). The saturated depth thus corresponds to the depth along which the plastic strain is saturated. The affected depth corresponds to the depth along which plastic strain is induced, regardless of its saturated or unsaturated nature. The affected depth is larger than the saturated depth. Their expressions are the following, without any particular consideration on the value of P :

$$l_{\text{sat}} = \frac{c_p c_e t_0}{c_e - c_p} \left\lfloor \frac{P}{2\sigma_{\text{hel}}} \right\rfloor \quad \text{and} \quad l_{\text{plast}} = \frac{c_p c_e t_0}{c_e - c_p} \left\lfloor \frac{P + \sigma_{\text{hel}}}{2\sigma_{\text{hel}}} \right\rfloor, \quad (38)$$

where the notation $\lfloor \cdot \rfloor$ denotes the floor function. In our case we find, using the x – t diagram of Figure 7:

$$l_{\text{sat}} = \frac{c_p c_e t_0}{c_e - c_p} \quad \text{and} \quad l_{\text{plast}} = 2l_{\text{sat}}, \quad (39)$$

which is in agreement with Equation (38). However we show that the plastic strain, at the surface, is saturated only for a limited period of time. Indeed, the interactions between the plastic and elastic fronts create a smaller secondary wave (corresponding to zone (g) in Figure 7(a)) that is propagating in the opposite direction as the initial wave. This secondary wave eventually reaches the left free surface boundary of the domain ($x = 0$), at which point it is reflected with an opposite sign. The opposite sign makes the wave generate new plastic strain in a zone where it was previously saturated. The plastic strain at the surface is saturated for $t \in [t_1, t_2]$, with

$$t_1 = t_0 \quad \text{and} \quad t_2 = \frac{t_0 (c_e^2 + c_p^2)}{c_p (c_e - c_p)}. \quad (40)$$

The new plastic strain taking place over the saturated plastic strain is dependent on the applied pressure (see lines 6 and 8 of Table 5), and is thus in this sense not saturated. These results are due to the perfectly plastic nature of the material model and may change if one considers hardening.

The present paper also improves the work of Ballard [3], mainly concerning the structure of the $x-t$ diagram of Figure 7(a) and the plastic strain distribution. We present here the full description of the stress wave propagation for $P = 5$ GPa, with complex reflection patterns, leading to the plastic strain being modified in several zones after the initial plastic loading, more specifically by the loading fronts identified by the numbers 4, 5, 6, 7 and 8 in Figure 7(a). Even though the work of Heuzé [14] tackles the same problem, it is modeled using a bar model, which is different from our uniaxial strain hypothesis, and does not result in the same stress wave propagation. These particularities of the stress wave propagation are confirmed by the numerical results, especially the GHR scheme (see for instance Figure 8(e) and (f)). Even if these features do not change the plastic affected depth, they change the plastic strain distribution, which eventually influences the residual stress distribution. Similar considerations in a general case on the stress and velocity can be found in Wang [15] (see Figure 7.5 of their work), without however any quantitative information about the plastic strain values.

The results of the case $P > (c_e + 5c_p)/(c_e + c_p)\sigma_{\text{hel}}$ are however not valid for any P . If P increases too much, the structure of the corresponding $x-t$ diagram will change, and with it the whole exact solution. The situation will be different if the wave front between zones (f) and (l) becomes fully plastic. This will be true if $\sigma_{(f)} > 2\sigma_{\text{hel}}$ (see Table 4), leading to:

$$P > 2\sigma_{\text{hel}} \frac{c_e + 3c_p}{c_e + c_p}. \quad (41)$$

For the sake of simplicity, we chose not to include the analysis of this case in this paper, which already covers most of the pressure range reachable in LSP for the chosen material. However, the change of structure of the exact solution implied by Equation (41) was verified numerically. Ballard [3] also proposed a pressure limit above which the material starts to behave hydrodynamically, where a simple elastic behavior is not enough to describe the material, which needs to make use of an equation of state [24, 33]. This condition reads:

$$P \lesssim 0.1\kappa. \quad (42)$$

In our case, $0.1\kappa = 17.5$ GPa, while the maximum applied pressure was 5 GPa.

The plastic strain profiles of Figures 4(e) and 4(f) present large values close to $x = 0$ diverging from the exact solution. These plastic strain values can be linked to the sharp nature of the loading profile, which induces large stress time increments in the very first steps of the simulation, and thus large plastic strain time increments. Later in the simulation, the plastic fronts become less sharp or smaller than the one in the initial instants, leading to smaller stress time increments and thus to smaller plastic strain time increments in accordance with Equation (24). To illustrate the influence of the sharpness of the pressure time profile, we can compute the plastic strain field induced by a pressure time profile of amplitude 2 GPa (to replicate the conditions of Figure 4), whose edges have been smoothed. The results are computed for the Lax–Wendroff and Godunov with High Resolution schemes, since they are the ones with the least amount of artificial viscosity. The results are presented in Figure 11. For both schemes, the plastic strains close to the edge of the domain are reduced once a smoother profile is used, though not entirely eliminated. It could be achieved by increasing the sampling of the time profile, which however implies to reduce the time increment of the simulation in order to get more point in the rise and decrease part of the profile. Here the discretization of the time profiles in Figure 11(a) corresponds exactly to the time increment Δt used in the simulations. However the smoothed version of the time profiles presents the disadvantage of producing stress waves that are more quickly attenuated, resulting in lower plastically affected depths. This makes the comparison with the exact solution less relevant, since the latter assume a instantaneous loading of the material.

The exact solution presented in this work relies on some necessary hypotheses (uniaxial strain field, perfectly plastic material, pressure loading as a step function) that may not be met in actual

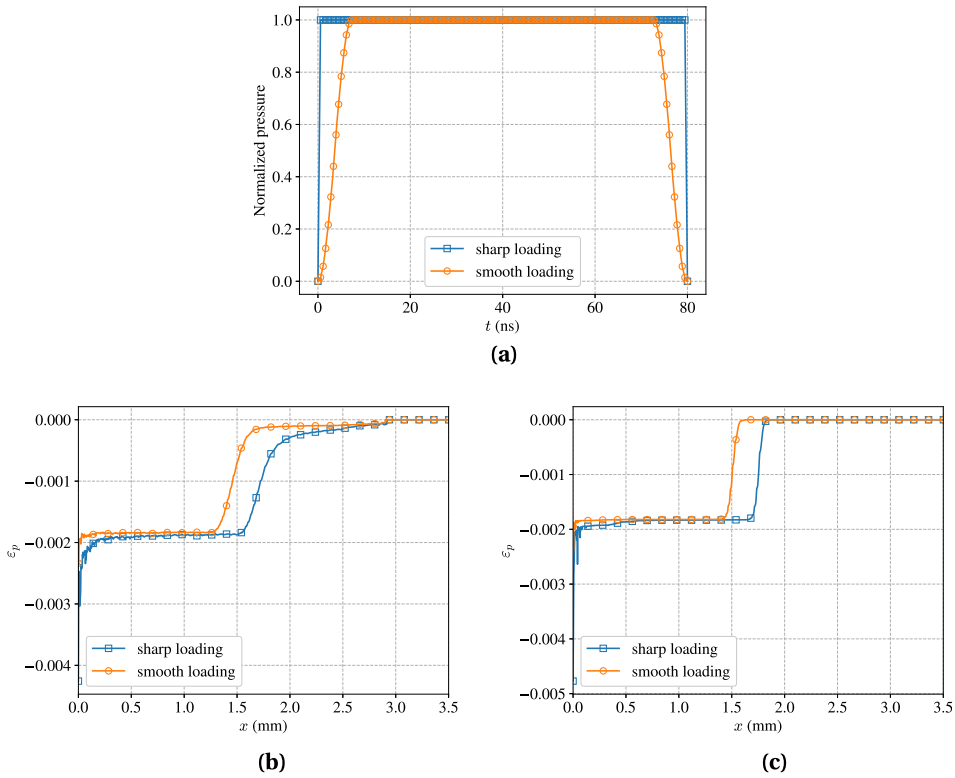


Figure 11. Comparisons of the plastic strain fields obtained with a sharp and smooth pressure time profile. (a) Different pressure time profiles. (b) Plastic strain fields computed with the Lax–Wendroff scheme. (c) Plastic strain fields computed with the Godunov with High Resolution scheme.

LSP configuration. Nonetheless, this solution provides insight and explanations to phenomenon that can be observed during LSP. The solution is also useful from a numerical point of view, to assess the quality of a numerical solution, before it is applied to more realistic modeling hypotheses. An important hypothesis in this work that allowed the computation of analytic stress and velocity fields is the step time pressure loading (limiting the number of characteristic lines needed for the x – t diagrams). Actual experimental pressure time profiles are smoother [34], and the exact fields are likely to overestimate the actual fields.

Finally, it is worth reminding that the expressions of the final displacement of the surface of the specimen in Equations (36) and (37) are valid in this uniaxial case, but may not be directly comparable to experimental (e.g. profilometry) or even 3D numerical results. Indeed, because of the edge effects originating at the edge of the laser spot and propagating inward [24, 29], a secondary velocity wave passes through the center of the impact, modifying the displacement field. This phenomenon cannot be represented with the current uniaxial model, and thus discrepancies can be expected when comparing its results to experimental data.

6. Conclusion

This article tackled the exact solution for the stress and velocity wave induced by laser shock peening, as well as the induced plastic strain and residual stress fields. This paper extends the

work of Ballard [3]. To achieve this, the elasto-plastic stress wave equation was first derived for uniaxial strains in an elastic perfectly plastic material. It was then showed that the hyperbolic nature of the stress wave equation allowed the determination of an exact solution using the methods of characteristics. It also allows the use of several dedicated numerical schemes to compute a numerical solution, each with its own numerical properties. Comparisons between the exact and numerical solutions were made for two different loading amplitudes, each one leading to a different architecture of the stress wave. It was shown that even though all numerical methods were able to correctly reproduce the exact solution, only the Godunov with High Resolution was able to capture the finest feature of the exact results. The plastic strains results were used to estimate the residual stress field, with an exact analytic formulation and with numerical results, both being in agreement. This work can thus be used to compute an initial estimation of the mechanical fields without any need of numerical computation. It can also be used to verify the precision of different numerical methods. An improvement of this work would be to determine the next analytical configuration for the $x-t$ diagram in case the pressure is much higher than the Hugoniot elastic limit, but being still realistic for LSP application, and without stepping into the hydrodynamic regime. Applying the method for smoother loading profiles is also possible, but the latter must be discretized into several step-wise constant portions.

Declaration of interests

The authors do not work for, advise, own shares in, or receive funds from any organization that could benefit from this article, and have declared no affiliations other than their research organizations.

Acknowledgments

This research was partly funded by the Carnot Institute ARTS and by the French Agence Nationale de la Recherche (ANR), research project ForgeLaser (grant number: ANR-18-CE08-0026).

Appendix A. Exact expressions of the parameters α and β for the evaluation of the residual stresses in the case $P > \sigma_{\text{hel}}$

$$\left\{ \begin{array}{l} \alpha = \frac{1}{L^3 \kappa (c_e - c_p)^2 (c_e + c_p)^7} \left[c_p t_0 \left(L \left[P \left(-c_e^9 - 7c_e^8 c_p - 20c_e^7 c_p^2 - 28c_e^6 c_p^3 - 14c_e^5 c_p^4 + 14c_e^4 c_p^5 \right. \right. \right. \right. \\ \quad \left. \left. \left. + 28c_e^3 c_p^6 + 20c_e^2 c_p^7 + 7c_e c_p^8 + c_p^9 \right) + 2\sigma_{\text{hel}} \left(3c_e^9 - 15c_e^8 c_p + 20c_e^7 c_p^2 + 60c_e^6 c_p^3 + 2c_e^5 c_p^4 - 10c_e^4 c_p^5 \right. \right. \right. \\ \quad \left. \left. \left. - 12c_e^3 c_p^6 - 36c_e^2 c_p^7 - 13c_e c_p^8 + c_p^9 \right) \right] + t_0 \left[P \left(5c_e^9 c_p + 36c_e^8 c_p^2 + 112c_e^7 c_p^3 + 196c_e^6 c_p^4 + 210c_e^5 c_p^5 \right. \right. \right. \\ \quad \left. \left. \left. + 140c_e^4 c_p^6 + 56c_e^3 c_p^7 + 12c_e^2 c_p^8 + c_e c_p^9 \right) + 2\sigma_{\text{hel}} \left(-4c_e^{10} + 23c_e^9 c_p - 102c_e^8 c_p^2 + 10c_e^7 c_p^3 - 342c_e^6 c_p^4 \right. \right. \right. \\ \quad \left. \left. \left. - 280c_e^5 c_p^5 - 146c_e^4 c_p^6 - 138c_e^3 c_p^7 - 46c_e^2 c_p^8 + c_e c_p^9 \right) \right] \right] \\ \beta = \frac{1}{6L^2 \kappa (c_e - c_p)^2 (c_e + c_p)^7} \left[-c_p t_0 \left(L \left[4P \left(-c_e^9 - 7c_e^8 c_p - 20c_e^7 c_p^2 - 28c_e^6 c_p^3 - 14c_e^5 c_p^4 + 14c_e^4 c_p^5 \right. \right. \right. \right. \right. \\ \quad \left. \left. \left. + 28c_e^3 c_p^6 + 20c_e^2 c_p^7 + 7c_e c_p^8 + c_p^9 \right) + 8\sigma_{\text{hel}} \left(3c_e^9 - 15c_e^8 c_p + 20c_e^7 c_p^2 + 60c_e^6 c_p^3 + 2c_e^5 c_p^4 - 10c_e^4 c_p^5 \right. \right. \right. \\ \quad \left. \left. \left. - 12c_e^3 c_p^6 - 36c_e^2 c_p^7 - 13c_e c_p^8 + c_p^9 \right) \right] + t_0 \left[P \left(15c_e^9 c_p + 108c_e^8 c_p^2 + 336c_e^7 c_p^3 + 588c_e^6 c_p^4 + 630c_e^5 c_p^5 \right. \right. \right. \\ \quad \left. \left. \left. + 420c_e^4 c_p^6 + 168c_e^3 c_p^7 + 36c_e^2 c_p^8 + 3c_e c_p^9 \right) + 6\sigma_{\text{hel}} \left(-4c_e^{10} + 23c_e^9 c_p - 102c_e^8 c_p^2 + 10c_e^7 c_p^3 \right. \right. \right. \\ \quad \left. \left. \left. - 342c_e^6 c_p^4 - 280c_e^5 c_p^5 - 146c_e^4 c_p^6 - 138c_e^3 c_p^7 - 46c_e^2 c_p^8 + c_e c_p^9 \right) \right] \right]. \end{array} \right. \quad (\text{A43})$$

Appendix B. Expression of the fluxes for the numerical schemes

We detail here the expression of the fluxes of Equation (23). They can be found in Leveque [22].

B.1. Lax–Friedrichs

The Lax–Friedrichs flux reads:

$$\mathbf{F}_{i-1/2}^n = \frac{1}{2} \mathbf{A}(\mathbf{U}_{i-1}^n + \mathbf{U}_i^n) - \frac{\Delta x}{2\Delta t} (\mathbf{U}_i^n - \mathbf{U}_{i-1}^n) \quad (\text{B44})$$

However to ensure stability, the complete scheme must be:

$$\mathbf{U}_i^{n+1} = \frac{1}{2} (\mathbf{U}_{i+1}^n + \mathbf{U}_{i-1}^n) - \frac{\Delta t}{2\Delta x} \mathbf{A}(\mathbf{U}_{i+1}^n - \mathbf{U}_{i-1}^n). \quad (\text{B45})$$

B.2. Lax–Wendroff

The Lax–Wendroff flux reads:

$$\mathbf{F}_{i-1/2}^n = \frac{1}{2} \mathbf{A}(\mathbf{U}_{i-1}^n + \mathbf{U}_i^n) - \frac{1}{2} \frac{\Delta t}{\Delta x} \mathbf{A}^2 (\mathbf{U}_i^n - \mathbf{U}_{i-1}^n). \quad (\text{B46})$$

B.3. Godunov

The expression for the Godunov flux is:

$$\mathbf{F}_{i-1/2}^n = \mathbf{A}^+ \mathbf{U}_{i-1}^n + \mathbf{A}^- \mathbf{U}_i^n. \quad (\text{B47})$$

Matrices \mathbf{A}^+ and \mathbf{A}^- are obtained in the following manner:

$$\mathbf{A}^+ = \mathbf{P} \mathbf{D}^+ \mathbf{P}^{-1} \quad \text{and} \quad \mathbf{A}^- = \mathbf{P} \mathbf{D}^- \mathbf{P}^{-1}, \quad (\text{B48})$$

with \mathbf{D}^+ and \mathbf{D}^- being diagonal matrices such that $(\mathbf{D}^+)_{ii} = \max(\gamma^{(i)}, 0)$ and $(\mathbf{D}^-)_{ii} = \min(\gamma^{(i)}, 0)$. $\gamma^{(i)}$ are the eigenvalues of \mathbf{A} and \mathbf{P} the matrix containing the eigenvectors of \mathbf{A} .

B.4. Godunov with high resolution

The Godunov with High Resolution scheme is similar to the standard Godunov scheme:

$$\mathbf{F}_{i-1/2}^n = \mathbf{A}^+ \mathbf{U}_{i-1}^n + \mathbf{A}^- \mathbf{U}_i^n + \tilde{\mathbf{F}}_{i-1/2}^n. \quad (\text{B49})$$

The expression of $\tilde{\mathbf{F}}_{i-1/2}^n$ is:

$$\tilde{\mathbf{F}}_{i-1/2}^n = \frac{1}{2} \sum_p |\gamma^{(p)}| \left(1 - \frac{\Delta t}{\Delta x} |\gamma^{(p)}| \right) \tilde{\alpha}_{i-1/2}^{(p)} \mathbf{r}^{(p)}, \quad (\text{B50})$$

where $\mathbf{r}^{(p)}$ is the p th eigenvector of \mathbf{A} , and $\tilde{\alpha}_{i-1/2}^{(p)}$ is given by:

$$\tilde{\alpha}_{i-1/2}^{(p)} = \alpha_{i-1/2}^{(p)} \phi(\theta_{i-1/2}^{(p)}), \quad (\text{B51})$$

with $\alpha_{i-1/2}^{(p)} = (\mathbf{P}^{-1}(\mathbf{U}_i - \mathbf{U}_{i-1}))_p$. In this equation, ϕ is a function called a flux limiter. In this work we consider the Superbee flux limiter which reads:

$$\phi(\theta) = \max(0, \min(1, 2\theta), \min(2, \theta)). \quad (\text{B52})$$

Finally in our case:

$$\theta_{i-1/2}^{(p)} = \frac{\alpha_{i-1/2}^{(p)}}{\alpha_{i-1/2}^{(p)}}, \quad (\text{B53})$$

with

$$I = \begin{cases} i-1 & \text{if } \gamma^{(p)} > 0 \\ i+1 & \text{if } \gamma^{(p)} < 0 \end{cases}. \quad (\text{B54})$$

References

- [1] K. Ding, L. Ye, *Laser Shock Peening Performance and Process Simulation*, Woodhead Publishing Limited, Cambridge, UK, 2006.
- [2] P. Peyre, R. Fabbro, P. Merrien, H. Lieurade, "Laser shock processing of aluminium alloys. Application to high cycle fatigue behaviour", *Mater. Sci. Eng. A* **210** (1996), p. 102-113.
- [3] P. Ballard, "Contraintes résiduelles induites par impact rapide. Application au choc laser", Phd thesis, Ecole Polytechnique, 1991.
- [4] P. Ballard, J. Fournier, R. Fabbro, J. Frelat, "Residual stresses induced by laser-shocks", *J. Phys. IV* **01** (1991), p. C3-487-C3-494.
- [5] W. Braisted, "Finite element simulation of laser shock peening", *Int. J. Fatigue* **21** (1999), p. 719-724.
- [6] E. Julan, C. Stolz, S. Tahéri, P. Peyre, P. Gilles, "Simulation of laser peening for generation of a surface compressive stresses", in *21e Congrès Français de Mécanique*, 2013, p. 6.
- [7] P. Peyre, I. Chaieb, C. Braham, "FEM calculation of residual stresses induced by laser shock processing in stainless steels", *Modell. Simul. Mater. Sci. Eng.* **15** (2007), p. 205-221.
- [8] P. Peyre, A. Sollier, I. Chaieb, L. Berthe, E. Bartnicki, C. Braham, R. Fabbro, "FEM simulation of residual stresses induced by laser Peening", *Eur. Phys. J. Appl. Phys.* **23** (2003), p. 83-88.
- [9] Y. Xiang, R. Mei, S. Wang, F. Azad, L. Zhao, S. Su, "Numerical investigation of the effect of laser shock peening parameters on the residual stress and deformation response of 7075 aluminum alloy", *Optik* **243** (2021), article no. 167446.
- [10] R. A. Brockman, W. R. Braisted, S. E. Olson, R. D. Tenaglia, A. H. Clauer, K. Langer, M. J. Shepard, "Prediction and characterization of residual stresses from laser shock peening", *Int. J. Fatigue* **36** (2012), p. 96-108.
- [11] L. Lapostolle, K. Derrien, L. Morin, L. Berthe, O. Castelnau, "Modeling and simulation of laser shock waves in elasto-plastic 1D layered specimens", *Int. J. Solids Struct.* **239-240** (2022), article no. 111422.
- [12] L. Lapostolle, L. Morin, K. Derrien, L. Berthe, O. Castelnau, "Modeling and simulation of laser shock waves in elasto-plastic polycrystalline microstructures", *J. Mech. Phys. Solids* **176** (2023), article no. 105310.
- [13] L. Lapostolle, L. Morin, K. Derrien, L. Berthe, O. Castelnau, "Fast numerical estimation of residual stresses induced by laser shock peening", *Eur. J. Mech. A/Solids* **97** (2023), article no. 104844.
- [14] T. Heuzé, "Lax-Wendroff and TVD finite volume methods for unidimensional thermomechanical numerical simulations of impacts on elastic-plastic solids", *J. Comput. Phys.* **346** (2017), p. 369-388.
- [15] L. Wang, *Foundations of Stress Waves*, Elsevier Science, Oxford, UK, 2007.
- [16] L. L. Wang, "Unloading waves and unloading failures in structures under impact loading", *Int. J. Impact Eng.* **30** (2004), p. 889-900.
- [17] A. M. Korsunsky, "The modelling of residual stresses due to surface peening using eigenstrain distributions", *J. Strain Anal. Eng. Des.* **40** (2005), p. 817-824.
- [18] M. Gelineau, "Etude de l'impact du grenaillage sur des composants mécaniques industriels à géométrie complexe", Phd thesis, Ecole Nationale Supérieure des Arts et Métiers, 2018.
- [19] D. Johns, *Thermal Stress Analyses*, Pergamon Press, Oxford, UK, 1965.
- [20] F. Ahdad, M. Desvignes, "Contraintes résiduelles et déformations plastiques: Leurs relations mutuelles pour des pièces de géométrie simple", *Matér. Tech.* **84** (1996), p. 46-50.
- [21] D. Glaser, C. Polese, A. Venter, D. Marais, J. Plaisier, "Evaluation of laser shock peening process parameters incorporating Almen strip deflections", *Surf. Coat. Technol.* **434** (2022), article no. 128158.
- [22] R. J. Leveque, *Finite Volume Methods for Hyperbolic Problems*, Cambridge University Press, Cambridge, UK, 2002.
- [23] F. Wang, G. James G., W. G. John, J. P. Bradley, H. S. David, "A conservative eulerian numerical scheme for elastoplasticity and application to plate impact problems", *Impact Comput. Sci. Eng.* **5** (1993), p. 285-308.
- [24] M. Ayad, L. Lapostolle, A. Rondepierre, C. Le Bras, M. Scius-Bertrand, S. Ünaldi, U. Trdan, Y. Rouchausse, J. Grassy, T. Maillot, V. Lapoujade, C. Michel, L. Berthe, "Modeling of multi-edge effects in the case of laser shock loadings applied on thin foils: Application for material characterization of aluminum alloys", *J. Appl. Phys.* **131** (2022), article no. 095902.
- [25] R. Seddik, A. Rondepierre, S. Prabhakaran, L. Morin, V. Favier, T. Palin-Luc, L. Berthe, "Identification of constitutive equations at very high strain rates using shock wave produced by laser", *Eur. J. Mech. - A/Solids* **92** (2022), article no. 104432.
- [26] Y. Hu, C. Gong, Z. Yao, J. Hu, "Investigation on the non-homogeneity of residual stress field induced by laser shock peening", *Surf. Coat. Technol.* **203** (2009), p. 3503-3508.
- [27] H. Kamkarrad, S. Narayanswamy, "FEM of residual stress and surface displacement of a single shot in high repetition laser shock peening on biodegradable magnesium implant", *J. Mech. Sci. Technol.* **30** (2016), p. 3265-3273.
- [28] M. Achintha, D. Nowell, "Eigenstrain modelling of residual stresses generated by laser shock peening", *J. Mater. Process. Technol.* **211** (2011), p. 1091-1101.
- [29] R. Ecault, F. Touchard, M. Boustie, L. Berthe, N. Dominguez, "Numerical modeling of laser-induced shock experi-

- ments for the development of the adhesion test for bonded composite materials”, *Compos. Struct.* **152** (2016), p. 382-394.
- [30] L. Lapostolle, “Etude numérique de l’influence d’hétérogénéités microstructurales sur les contraintes résiduelles induites par choc laser”, Phd thesis, Arts et Métiers, Paris, 2022.
- [31] C. Cellard, D. Retraint, M. François, E. Rouhaud, D. Le Saunier, “Laser shock peening of Ti-17 titanium alloy: Influence of process parameters”, *Mater. Sci. Eng. A* **532** (2012), p. 362-372.
- [32] M. Ayad, L. Lapostolle, A. Rondepierre, C. L. Bras, S. Unaldi, C. Donik, D. Klobcar, L. Berthe, U. Trdan, “New methodology of dynamical material response of dissimilar FSWed Al alloy joint under high strain rate laser shock loading”, *Mater. Des.* **222** (2022), article no. 111080.
- [33] P. Peyre, L. Berthe, V. Vignal, I. Popa, T. Baudin, “Analysis of laser shock waves and resulting surface deformations in an Al–Cu–Li aluminum alloy”, *J. Phys. D: Appl. Phys.* **45** (2012), article no. 335304.
- [34] M. Scius-Bertrand, L. Videau, A. Rondepierre, E. Lescoute, Y. Rouchasse, J. Kaufman, D. Rostohar, J. Brajer, L. Berthe, “Laser induced plasma characterization in direct and water confined regimes: new advances in experimental studies and numerical modelling”, *J. Phys. D: Appl. Phys.* **54** (2021), article no. 055204.